

Image Compression Using Novel View Synthesis Priors

Luyuan Peng, *Member, IEEE*, Mandar Chitre, *Senior Member, IEEE*, Hari Vishnu, *Senior Member, IEEE*, Yuen Min Too, *Member, IEEE*, Bharath Kalyan, *Senior Member, IEEE*, Rajat Mishra, *Member, IEEE* and Soo Pieng Tan

Abstract—Real-time visual feedback is essential for tetherless control of remotely operated vehicles, particularly during inspection and manipulation tasks. Though acoustic communication is the preferred choice for medium-range communication underwater, its limited bandwidth renders it impractical to transmit images or videos in real-time. To address this, we propose a model-based image compression technique that leverages prior mission information. Our approach employs trained machine-learning based novel view synthesis models, and uses gradient descent optimization to refine latent representations to help generate compressible differences between camera images and rendered images. We evaluate the proposed compression technique using a dataset from an artificial ocean basin, demonstrating superior compression ratios and image quality over existing techniques. Moreover, our method exhibits robustness to introduction of new objects within the scene, highlighting its potential for advancing tetherless remotely operated vehicle operations.

Index Terms—underwater, image compression, 3D gaussian splatting, remotely operated vehicle, acoustic communication.

I. INTRODUCTION

UNDERWATER missions, such as deep-sea exploration, environmental monitoring, and infrastructure inspection and manipulation, heavily rely on remotely operated vehicles (ROVs) [1]–[3]. Traditional ROVs are tethered to a surface platform, which provides a continuous power supply, enabling extended operation. The tether also serves as a reliable two-way communication conduit, transmitting control commands to the ROV and sending sensor data, video feed, and other information back to the operators [4]. However, the tether imposes significant limitations on ROV operations. It restricts the ROV’s maneuverability, limiting its ability to navigate through tight spaces or complex underwater environments [5]. This constraint can hinder the ROV from reaching certain areas or performing delicate tasks. Additionally, the tether poses a significant risk of entanglement with underwater structures and obstacles such as rocks or reefs, potentially trapping the ROV or complicating retrieval, which could lead to mission failure or loss of the vehicle. Moreover, the tether’s weight and bulk add to the logistical challenges of deploying and recovering the ROV. This often necessitates additional equipment, such as winches and cable reels, further increasing the operational complexity.

To mitigate these challenges, the development of tetherless ROVs has been a focus in marine robotics [5], with one of the greatest challenges being real-time wireless underwater communication between the ROV and the surface platform. Radio waves, while delivering high data rates and low latency

in terrestrial environments, propagate poorly underwater due to high attenuation, making them unsuitable for underwater communication [6]. Instead, acoustic communication is a commonly used solution due to its long range and low power consumption, though its bandwidth is limited [7].

To enhance underwater wireless communication, much work has been done to improve the data rate of acoustic links [8]. In recent years, optical communication has also been explored as an alternative to acoustic communication, offering higher data rates but limited range [9]. Current state-of-the-art acoustic links offer bit rates on the order of tens of kilobits per second (kbps) at distances of several hundred meters to a few kilometers, depending on channel conditions [10], [11]. Optical links, while capable of up to 10 megabits per second, have a limited range which may be worsened in turbid conditions, and are usually highly directional. While acoustic links can handle transmission of commands and some sensor data, their bandwidth is still inadequate for tasks such as real-time image transmission, which is crucial for operators to visualize the environment and control the ROV effectively, especially in inspection and manipulation tasks. As such, efficient image compression strategies are needed to enable real-time image transmission over acoustic links.

Image compression techniques reduce the amount of data required to represent an image. Classical image compression techniques can be broadly categorized into lossless and lossy compression. Lossless compression techniques, such as PNG and GIF, remove spatial and coding redundancies in images, prioritizing reconstruction of the original image at the cost of compression ratio. Lossy compression techniques, such as JPEG and WebP, remove also psychovisual redundancies and thus achieve high compression ratios while maintaining good image quality. While lossy compression techniques are effective for general-purpose image compression, they do not offer compression ratios high enough for real-time image transmission over limited-bandwidth acoustic links. For example, a 320×180 image compressed through WebP is still 3.5 kB or more, which means a 100 kbps link can only afford to transmit at most 3 key-frames per second. For a 1280×720 image, the compressed size is substantially larger, often exceeding 20 kB, which would reduce the transmission rate to less than one key-frame per second on the same 100 kbps link.

With the rise of machine learning, new image compression techniques have been developed that promise better performance than classical methods in either compression ratio or

image quality [12]–[19]. Early work focused on using multi-layer perceptrons to replace key components of classical image compression techniques [20]. Recent work has explored end-to-end image compression techniques that learn to compress images directly from data [18]. Most of these techniques are based on neural networks, which are trained to extract a low-dimensional latent space or feature vector from images and reconstruct them from the latent space using architectures such as autoencoders and generative adversarial networks. Using information learned from a large dataset, these neural networks can perform adaptive and content-aware compression and thus achieve high compression ratios while maintaining image quality comparable or superior to classical techniques. These techniques demonstrate that efficient image representations can be achieved through data-driven learning. However, they require large training datasets—which are unavailable for underwater inspection images—and lack the ability to incorporate specific scene knowledge.

In underwater inspection tasks, sufficient prior information often exists to enable efficient image compression. Inspections are frequently conducted at the same sites for routine monitoring, assessment, and maintenance, allowing us to gather prior knowledge of the environment. Additionally, predictable vehicle motion provides temporal correlations between images. Leveraging this available information enables more efficient image representations, facilitating real-time transmission in underwater inspections.

The recent advancements in novel view synthesis (NVS) have led to rise of differentiable techniques such as neural radiance fields (NeRFs) [21] and 3D Gaussian splatting (3DGS) [22], which learn to represent a 3D scene as a continuous function and can render realistic camera images from any viewpoint within the scene. This capability allows us to use an optimal latent representation for each camera image, which includes essential parameters such as camera pose and potentially other factors like lighting and color, to render the image using the differentiable NVS model. In our previous work [23], we proposed to use camera pose as the latent representation of camera images. To capture possible dynamic changes in the scene, we compressed the difference between the camera image and rendered images using classical lossy compression techniques and transmitted the compressed difference together with the latent representation. By transmitting the compressed difference along with the latent representation instead of the camera image, we can achieve high compression ratios while maintaining image quality, enabling real-time image transmission over limited-bandwidth acoustic links. However, rendered images do not always accurately match the camera images due to inaccuracy of the latent representation estimated by the neural network-based estimator or measured by sensors such as Inertial Measurement Unit and Doppler Velocity Logger [24]. To address this issue, our previous work computed an affine transformation of the rendered view that effectively preserves the salient features observed in the camera view. However, this is not an ideal solution, as the affine transform implicitly assumes a 2D world. The model mismatch manifests in terms of artifacts in the difference image, thus increasing the data size to be transmitted.

In this paper, our contributions are:

- 1) We propose an innovative NVS-based image compression approach that leverages gradient descent through trained NVS models. To the best of our knowledge, our work is the first time that NVS models have been utilized for image compression. Our method is computationally efficient, and achieves significantly higher compression ratios than classical lossy image compression techniques.
- 2) We conduct an in-depth examination of various loss functions, optimization algorithms, and initialization methods for NVS-based image compression approach. This analysis provides valuable insights into the factors affecting performance and guides the selection of optimal configurations for different scenarios.
- 3) We rigorously evaluate the performance of our proposed technique in a confined underwater environment. The results demonstrate that NVS-based image compression outperforms existing image compression methods in both compression ratio and image quality.
- 4) We assess the robustness of our method when encountering novel objects and occlusions within the scene from structures, both large and small. Our findings reveal that our method can effectively handle these cases, maintaining high image quality and reliability in dynamic underwater settings.

The paper is organized as follows. Section II provides an overview of our proposed image compression technique, a review of recent attempts to invert NVS models for latent representation estimation and an detailed description of our optimization strategy. Section III presents the dataset collected, and demonstrates robust performance of our proposed technique. Finally, Section IV concludes the paper and outlines future work.

II. METHODS

A. Overview of the Compression Framework

Our NVS-based compression technique reduces the size of data to be transmitted between the ROV and the operator using a NVS model trained with prior knowledge of the scene. The trained NVS model renders realistic images given an optimal latent representation which includes the camera pose and potentially other elements such as transient embeddings. These images can be rendered on the ROV and also at the operator end, thus serving as prior information that can be used for data compression. The only information that needs to be transmitted to the operator in order to reconstruct the camera view is (1) the optimal representation, and (2) the differences between the NVS-rendered image and the camera image, I_{diff} . We compress I_{diff} using lossy image compression methods.

The size of the compressed I_{diff} is largely determined by the accuracy of the latent representation - an offset of just a few pixels between the rendered and camera images can make the difference image size significant. While existing underwater image-based pose estimators [24]–[26] can achieve accuracy sufficient for navigation, these estimated latent representations

are often not accurate enough for image compression. Depending on the distance from the ROV to the object of interest, a small error in the latent representation can result in a large image difference between the camera image and the rendered image as shown in Fig. 1. As such, we propose an inverse NVS (dubbed *iNVS*) to search for the optimal latent representation that gives us the closest model-rendered image.

An overview of our approach is shown in Fig. 2.

B. Existing Work in Inverting NVS Models

Previous work has attempted to use gradient descent on the pose parameter provided to an NVS model (e.g., NeRF or 3DGS) for pose estimation. iNeRF [27] uses this approach to invert a camera image based on a trained NeRF model to estimate the camera pose, by minimizing the pixelwise difference between rendered and camera images via gradient descent. iComMa [28] proposes a similar approach using 3DGS models, minimizing both pixelwise differences in the image, which is the mean squared error (MSE) between each pixel in the camera image and the rendered image, and matching loss, which is the mean of Euclidean distances between keypoints in corresponding images, proposed as an alternative for enhanced robustness towards poor initialization. The MSE loss is defined as:

$$L_{\text{mse}} = \frac{1}{N} \sum_{i=1}^N (I_{\text{camera}}(i) - I_{\text{rendered}}(i))^2 \quad (1)$$

where I_{camera} and I_{rendered} are the camera image and the rendered image, respectively, $I(i)$ refers to the intensity of the i^{th} pixel, and N is the number of pixels in the image.

The matching loss is defined as:

$$L_{\text{match}} = \frac{1}{M} \sum_{i=1}^M (k_{\text{camera}}(i) - k_{\text{rendered}}(i))^2 \quad (2)$$

where k_{camera} and k_{rendered} are the corresponding keypoints in the camera image and the rendered image, respectively, $k(i)$ refers to the i^{th} keypoint, and M is the number of keypoints.

Both iNeRF and iComMa use the Adam optimizer [29] for pose optimization. While iComMa has an improved speed over iNeRF due to faster convergence and high rendering speed of 3DGS models, it still requires about a second for one optimization on a single NVIDIA RTX A6000 GPU, which is prohibitively too slow for the video transmission speed required for tetherless control.

C. *iNVS*

iNVS aims to rapidly estimate the latent representation required to minimize the difference between the camera image and the 3DGS model-rendered image. The flow of *iNVS* is shown in Fig. 3. This optimization process relies on three key components: (1) an effective initialization strategy, (2) a fast optimization method, and (3) an appropriate objective function.

1) *Initialization strategy*: An effective initialization is crucial for the rapid convergence of optimization algorithms. In inspection missions where the vehicle moves slowly and

steadily, there are minimal changes in the latent representation between consecutive frames. Assuming such a scenario, we use the optimized latent representation from the previous frame as an initialization point for estimating the latent representation in the current frame, provided that a “good” previous frame exists. This approach leverages the small inter-frame variations in the latent representation, enabling faster convergence due to the proximity of the initial estimate to the true latent representation. By utilizing the optimized latent representation from the previous frame whenever possible, we mitigate the issues associated with sensor drift, biases, and estimator noise, providing a more accurate starting point for optimization.

To determine whether a previous frame is “good”, we compute the MSE between the normalized camera image and the normalized rendered image at the optimized latent representation from the previous frame, and compare it against a predetermined threshold.

When a “good” previous frame is unavailable, such as at the start of a mission, or when the MSE of previous frame exceeds the threshold, other initialization strategies can be used. In this paper, we employ a trained neural network-based estimator [24] to provide an initial estimate of the latent representation in such cases.

2) *Optimization method*: For the optimization method, we select the Broyden–Fletcher–Goldfarb–Shanno [30]–[33] (BFGS) algorithm to refine the latent representation. BFGS is a quasi-Newton method that approximates the Hessian matrix, which represents the second-order partial derivatives of the objective function, using gradient evaluations. This approximation enables the algorithm to iteratively update the parameters efficiently toward convergence. BFGS iterates on the initial latent representation to estimate the closest local minimum.

The choice of BFGS in this application is motivated by the deterministic nature of our problem, which involves a small number of parameters. Deterministic optimization methods like BFGS are more suitable in this context compared to stochastic methods designed for large-scale problems, such as Adam. In our case, the initialization is close to the optimal latent representation. In terms of optimization, this means it is in the vicinity of the global minimum on the cost surface, and thus the BFGS is able to obtain the optimal latent representation more efficiently as compared to stochastic methods.

3) *Objective Function*: To obtain a model-rendered image that is similar to the camera-image to within an error that is on the order of a few pixels, we can directly use the mean-square difference between the camera image and the rendered image as the objective function to minimize for the *iNVS* technique. We employ MSE, described in Eq. (1), as the objective function for *iNVS*. The MSE provides a straightforward measure of the difference between images and is computationally efficient to compute. While iComMa suggests that an objective function defined as a weighted sum of MSE and matching loss can improve robustness towards poor initialization, we find the process of keypoints extraction and matching too computationally expensive for real-time operation.

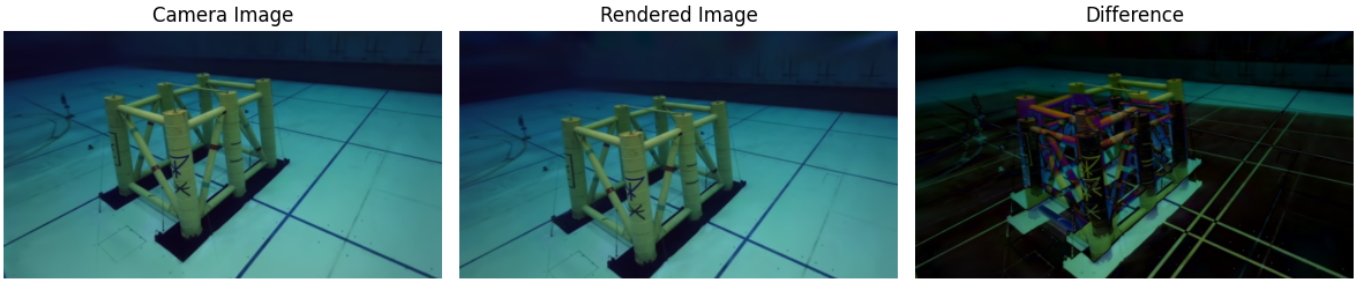
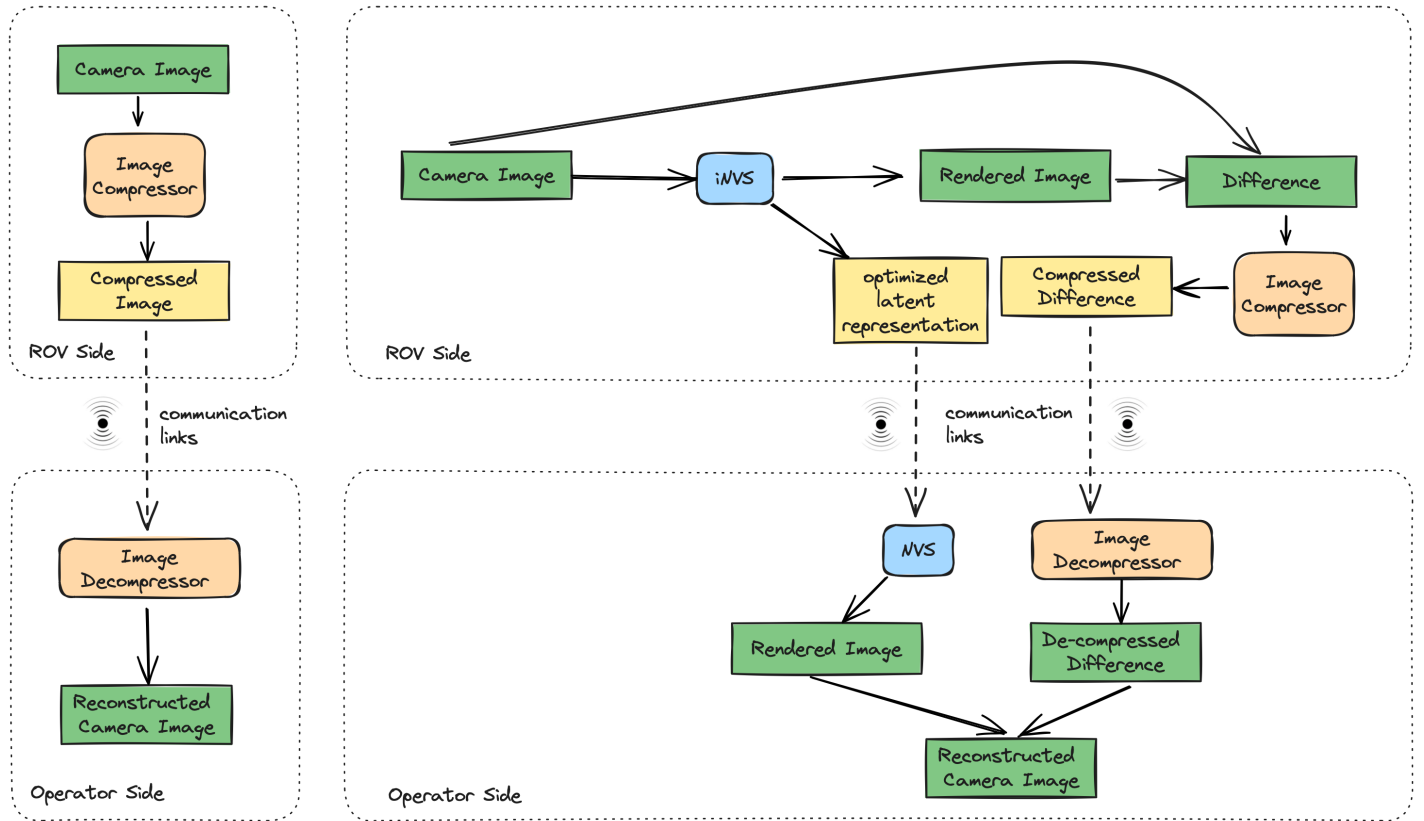


Fig. 1: Effect of a 5° rotation error on the rendered image. The left image is the camera image, the middle image is the image rendered at the latent representation rotated by 5° about the x-axis, and the right image is the difference between the two images.



(a) Overview of classical image compression method. The camera image is compressed using a lossy image compressor and then transmitted to the operator side where compressed image is reconstructed through the decompressor.

(b) Overview of the proposed NVS-based image compression technique. On the ROV side, given a camera image, we first perform iNVS to get the optimized latent representation and the corresponding rendered image. We then compute and compress the difference, I_{diff} between the rendered image and the camera image, using classical lossy image compressor. We transmit the compressed I_{diff} and optimized latent representation over the acoustic link. At the surface, we decompress the compressed I_{diff} and render the camera image from the optimized latent representation using the trained 3DGS model. Adding the decompressed I_{diff} to the rendered image, we obtain the reconstructed camera image.

Fig. 2: Classic image compression scheme and NVS-based image compression scheme.

4) *Implementation Details*: We select the 3DGS NVS model as the backbone of our technique, primarily due to its high rendering speed. Rendering a 320×180 image takes less than 50 milliseconds on an NVIDIA Jetson Orin using 3DGS, making it suitable for real-time image rendering and iterative optimization. In this paper, we use the camera pose as the latent representation to be optimized.

For training the 3DGS model and rendering images, we

use camera images collected in the initial survey run (the “mapping run”) as the training data and train a *splatfacto* model [34] provided by *nerfstudio* [35].

We train the neural network-based latent representation estimator, referred to as PoseLSTM, using the approach described in [24]. We utilize COLMAP [36], an open-source structure-from-motion software, to compute the latent representation associated with each image within an arbitrary reference

III. EXPERIMENTS

A. Dataset

We collected data from an artificial ocean basin at the Technology Center for Offshore and Marine, Singapore (TCOMS) [39], which is an indoor pool measuring $60 \text{ m} \times 48 \text{ m} \times 12 \text{ m}$. As illustrated in Fig. 4, we placed a yellow structure in the basin consisting of six piles interconnected by metallic pipes, with each pile comprising three metallic oil barrels. The overall dimensions of the structure were approximately $3.9 \text{ m} \times 4.6 \text{ m} \times 3.0 \text{ m}$.

We conducted three survey runs within this environment, where the ROV surveyed the structure using a similar lawn-mower trajectory in each trial. We refer to these trials as the mapping run (M1), test run 1 (T1), and test run 2 (T2). In M1, the ROV collected data for training the 3DGS model which forms the prior. In T1 and T2, we evaluate the performance of our proposed image compression technique using the model trained based on M1. As shown in Fig. 4c, during T2, a new metallic structure was placed next to the existing one to test the robustness of our technique towards novel objects in the scene.

We selected 1,422 images from M1 for training the 3DGS model and PoseLSTM, and sampled 1,000 consecutive images from each of T1 and T2 for evaluation. The images collected during the trials were color images with a resolution of 1280×720 pixels, captured at 3 frames per second. We downscaled these images to 320×180 pixels for transmission purposes, and the image compression is tested at this image resolution.

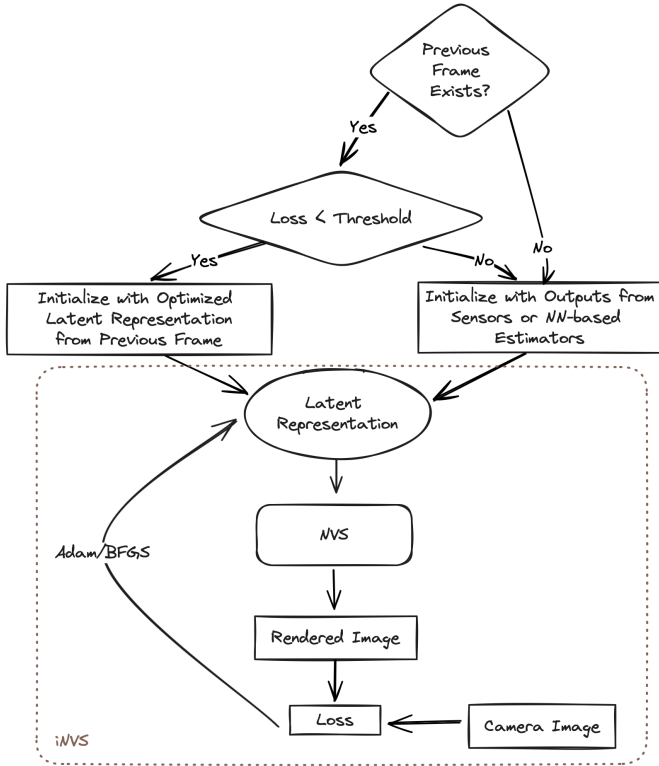


Fig. 3: Flow of iNVS.

coordinate system. The computed COLMAP representation and corresponding images serve as the training data for PoseLSTM.

To determine whether the estimated latent representation is accurate enough to initialize the next frame, we set a threshold of 1×10^{-3} on the MSE between the normalized camera image and the normalized NVS-rendered image at the optimized latent representation.

The BFGS algorithm is implemented using the *pytorch-minimize* package [37]. We set the gradient tolerance to 1×10^{-5} and the parameter tolerance to 1×10^{-6} to ensure convergence. For benchmarking purposes, we also implement the Adam optimizer using PyTorch, setting the initial learning rate to 1×10^{-3} and halving it if no loss reduction is observed for three consecutive epochs.

To compare with the matching loss (2) proposed as part of iComMa, we implement this approach using the same pretrained deep learning-based feature extractor, *LoFTR* [38], to extract and match keypoints, setting the number of keypoints to 20.

For benchmarking and compressing the difference image I_{diff} , we test using two standard image compression algorithms – WebP and JPEG-XL. This allows us to compare the performance of our method against classical lossy image compression techniques.

All our experiments were conducted using an NVIDIA RTX6000 Ada GPU.

B. Parametric Studies

We evaluate the performance of different loss functions, optimization methods, and initialization strategies for iNVS.

1) *Performance and robustness using MSE and Matching Loss*: In this subsection, we study the performance of iNVS with different objective functions, and how it varies with the error in the initial latent representation. We introduce perturbations to the latent representation to simulate initialization errors that occur during actual survey runs. For each perturbation, we randomly select either a translation or rotation axis and sample a perturbation value from a uniform distribution within specified ranges. Translation perturbations are sampled uniformly within $[-1.58 \text{ m}, 1.58 \text{ m}]$, and rotation perturbations are sampled uniformly within $[-40^\circ, 40^\circ]$. Using the perturbed latent representation as the initialization, we optimize the latent representation using either MSE loss or matching loss until convergence.

After optimization, we compute the Peak Signal-to-Noise Ratio (PSNR) of the rendered images compared to the camera images in dB, energy in I_{diff} and number of bytes of compressed I_{diff} between the camera image and rendered image at the optimized latent representation. We also record the number of iterations required for convergence. This process is repeated on the 1,422 images from M1. The results are shown in Fig. 5. The PSNR is defined as:

$$\text{PSNR} = 10 \cdot \log_{10} \left(\frac{1}{L_{\text{mse}}} \right) \quad (3)$$

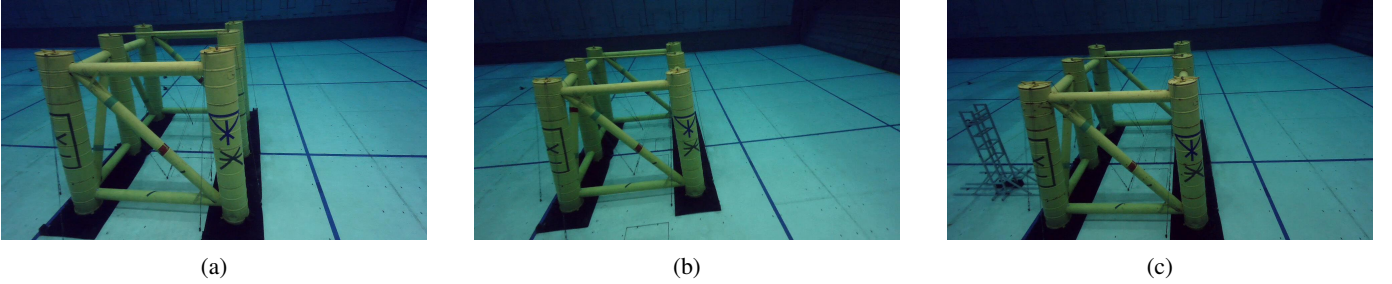


Fig. 4: Example images from the dataset: (a) An image from the mapping run (M1), showing the ROV surveying the original structure; (b) An image from test run 1 (T1), where the ROV continues to survey the same structure for performance evaluation; (c) An image from test run 2 (T2), featuring an additional metallic structure placed next to the original to test the robustness of our technique toward novel objects in the scene.

where L_{mse} is defined in Eq. (1).

The model trained using MSE loss outperforms that using matching loss across all metrics and perturbation values in terms of median performance, despite exhibiting higher variance. Overall, using MSE loss achieves a rendered image with higher PSNR and thus a more compressed I_{diff} than using matching loss. The larger variability in performance observed when using MSE loss is likely due to its sensitivity to initialization and the presence of more local minima in its loss landscape. Moreover, MSE loss converges faster than matching loss, even though it requires more iterations.

2) *Optimization Methods:* With the MSE loss as the objective function, we compare the performance of the BFGS and Adam optimization algorithms using a similar approach as described above. Additionally, we investigate the performance of a combined method, denoted as Adam+BFGS, where Adam is used as the optimizer until convergence, followed by BFGS for fine-tuning. This hybrid approach is a common practice in optimization. We present the results in Fig. 6. We find that both BFGS and Adam+BFGS outperform Adam across all three metrics and perturbation values. Adam+BFGS performs slightly better than BFGS at small translational perturbations; however, overall, BFGS achieves better performance than Adam+BFGS at higher perturbation levels. Adam+BFGS exhibits the smallest variance among all three optimization methods at high perturbations and hence better reliability.

Apart from exhibiting better median performance, BFGS also requires fewer iterations to converge than Adam and Adam+BFGS, and each of its iterations is faster. Therefore, we choose BFGS as the optimization method for iNVS henceforth.

It is important to note that the performance of iNVS degrades rapidly when the perturbations are large (e.g., greater than 1.3 m in translation or 37° in rotation). Therefore, a good initialization is crucial for the optimal performance of iNVS.

3) *Initialization:* We compare the convergence performance of iNVS using two initialization methods: (1) the latent representation estimated from the previous frame and (2) the latent representation estimated by PoseLSTM on the current frame. Our results show that initializing with the previous frame’s latent representation requires fewer iterations for convergence and is more computationally efficient, as it eliminates the need for neural network inference.

C. Compression performance

We evaluate the compression performance of our iNVS-based approach using dataset T1. For the first frame, the latent representation estimated by PoseLSTM is used as the initialization, and for subsequent frames, we use the latent representation for the previous frame. Our evaluation metrics include (1) compression ratio, (2) size (in bytes) of I_{diff} , and (3) the PSNR of the reconstructed image. We compare the performance of our method, iNVS, against classical compression methods on the raw image, specifically WebP and JPEG-XL. Additionally, we assess the impact of latent representation optimization by comparing the results from iNVS with those from the approach proposed in our previous work [23]. To implement the previous approach, we use the latent representation estimated by PoseLSTM as the input to the 3DGS model. We refer to this method as Pose+3DGS+Compressor. For both iNVS and Pose+3DGS+Compressor, we use either WebP or JPEG-XL for compressing I_{diff} . The results are reported in Table I.

Our results demonstrate that the iNVS-based approach achieves a significantly higher compression ratio than WebP and JPEG-XL while maintaining a higher PSNR. iNVS with WebP achieves the highest compression ratio of 160.95, which is 3.18 times higher than WebP and 5.14 times higher than JPEG-XL. The compressed data to be transmitted has an average size of 1.2 kB, which means we can transmit about 10 key-frames per second over a 100 kbps acoustic link using this approach.

iNVS with JPEG-XL achieves the highest PSNR of 36.15 dB, which is 2.85 dB higher than WebP and 2.58 dB higher than JPEG-XL. In Fig. 8a, we observe the reconstructed image from iNVS is clearer and sharper than the image compressed and decompressed by classical methods. The results demonstrate that our iNVS technique is more effective than classical compression methods for real-time image transmission over limited-bandwidth acoustic links.

We also find the performance of Pose+3DGS+Compressor is worse than both iNVS and classical compressors in terms of compression ratio, compressed size and PSNR. As illustrated in Fig. 9a and Fig. 9b, the error in the latent representation estimated by PoseLSTM often causes large differences between the camera image and the rendered image, compared

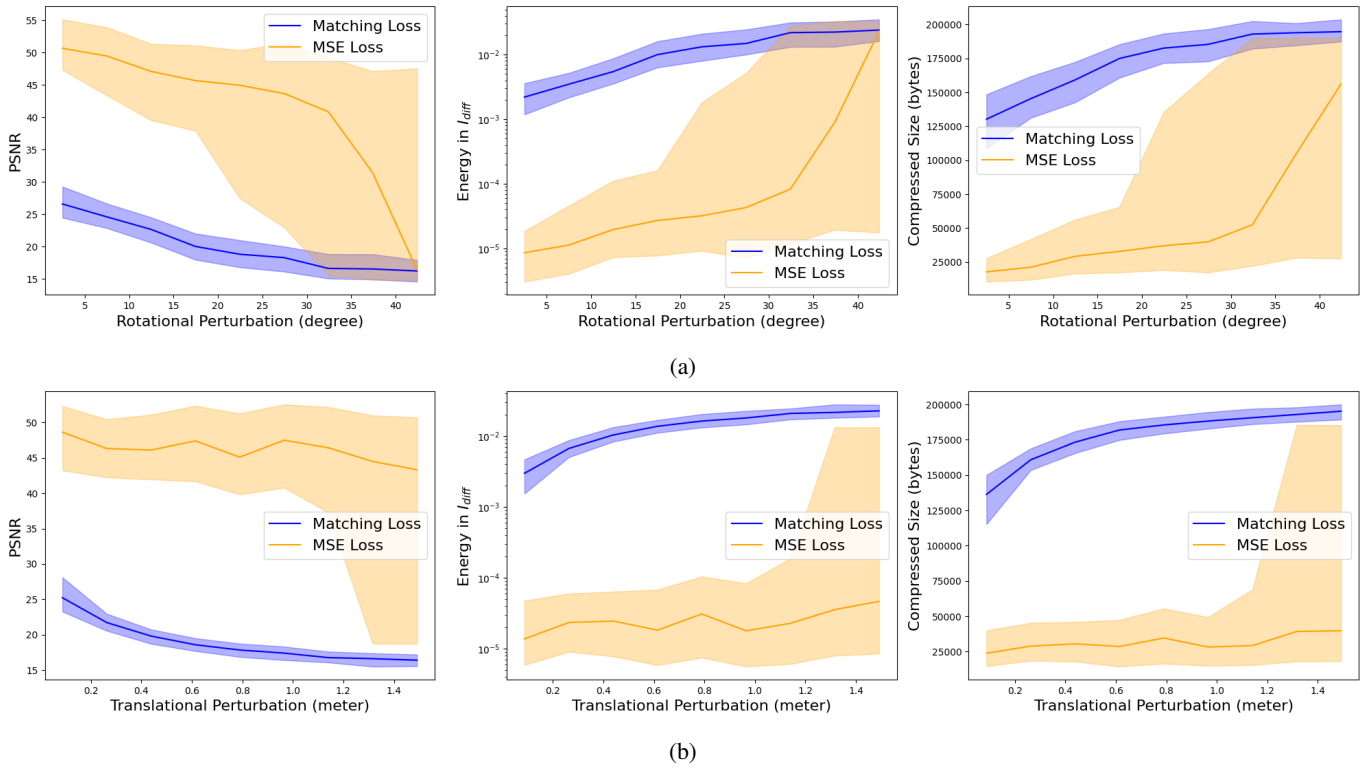


Fig. 5: Performance of MSE loss and Matching Loss at different perturbation. Panel (a) compares the performance at different rotational perturbation in initial latent representation. Panel (b) compares the performance at different translational perturbation.

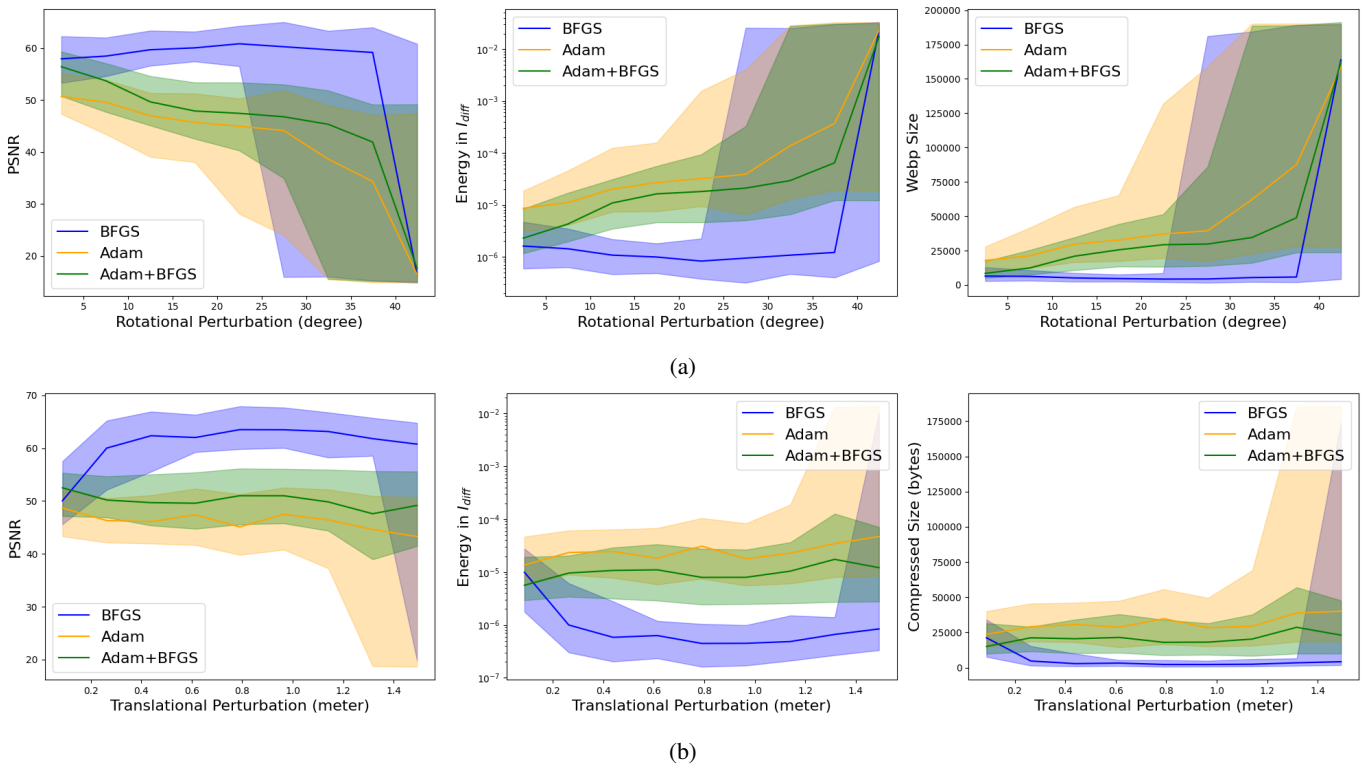


Fig. 6: Performance of Adam and BFGS at different perturbation. Panel (a) compares the performance at different rotational perturbation. Panel (b) compares the performance at different translational perturbation.

to the optimized latent representation by iNVS. This results in a much larger compressed size for Pose+3DGS+WebP than

TABLE I: Quantitative results on the datasets T1 and T2. The results are averaged over 1000 images. Arrows indicate the direction of improvement.

	T1			T2		
	Compression Ratio \uparrow	Compressed Size (bytes) \downarrow	PSNR \uparrow	Compression Ratio \uparrow	Compressed Size (bytes) \downarrow	PSNR \uparrow
WebP	49.04	3544.40	33.30	48.16	3654.88	33.43
JPEG-XL	30.38	5710.53	33.57	29.93	5827.21	33.86
Pose+3DGS+Compressor(WebP)	41.90	4164.39	31.85	39.66	4452.33	31.83
Pose+3DGS+Compressor (JPEG-XL)	39.43	4400.85	31.31	37.64	4629.30	31.37
iNVS (WebP)	156.21	1218.68	35.83	115.21	1651.06	35.32
iNVS (JPEG-XL)	120.27	1551.68	36.15	88.57	2072.83	35.55

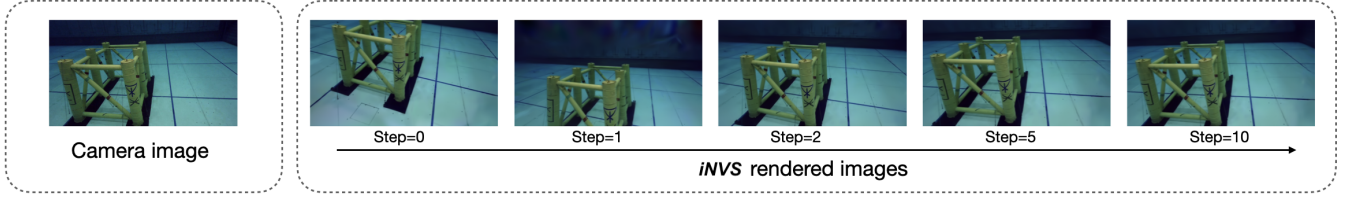


Fig. 7: iNVS optimization process. Given a camera image, iNVS rapidly and accurately optimizes the latent representation to minimize the difference between the camera image and the rendered image.

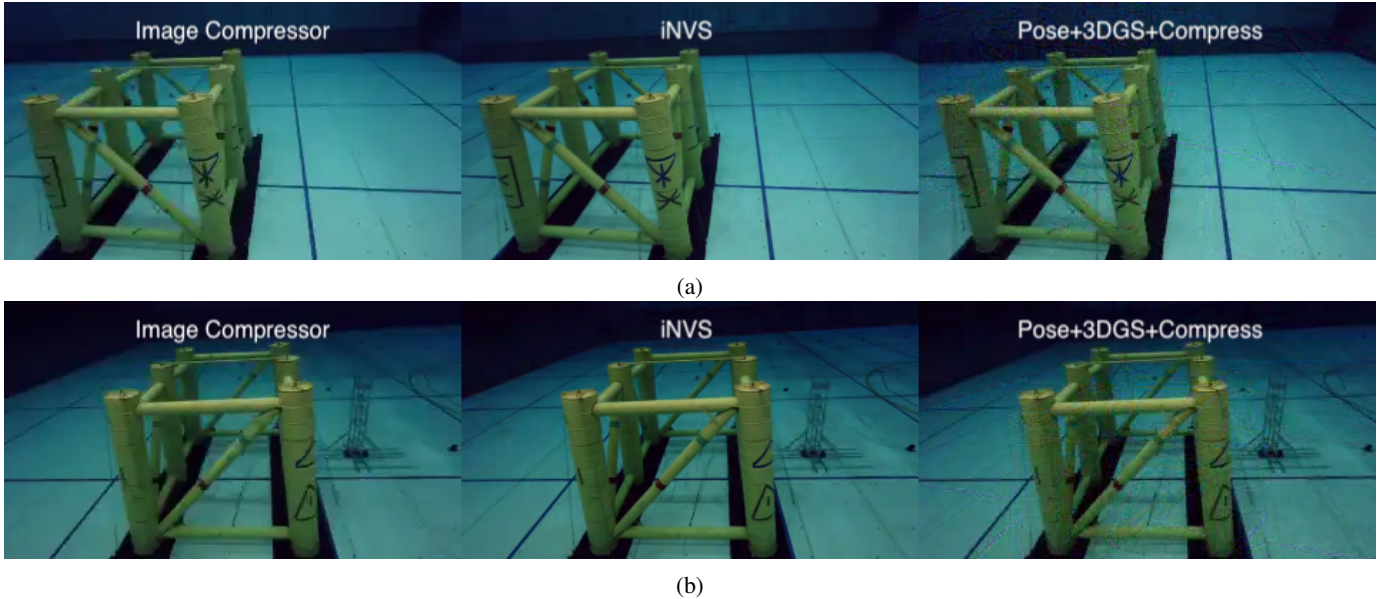


Fig. 8: Visualization of reconstruction quality for T1 and T2. Panel (a) shows the reconstructed images for T1 and panel (b) shows the reconstructed images for T2. The left image is the decompressed image by WebP, the middle image is the image reconstructed using iNVS, and the right image is the one reconstructed using Pose+3DGS+Compressor.

iNVS. As such, the latent representation estimation by iNVS is crucial for the performance of our technique.

In Fig. 7, we show an example of the iterative optimization process of iNVS. Given a camera image, iNVS rapidly and accurately optimizes the camera latent representation to minimize the difference between the camera image and the rendered image. The optimization process converges within a few iterations, demonstrating the efficiency and effectiveness of our technique.

D. Robustness to Novel Objects in the Scene

In inspection missions, it is common to encounter changes in the scene with time, such as the presence of additional structures or objects (e.g. fish, biological growth, corrosion, etc). We evaluate the robustness of our iNVS technique to novel objects in the scene using dataset T2, in a similar manner as described above.

We test the performance of iNVS on two examples, representing novel objects commonly encountered in inspection missions. The first is a thin yellow safety line that moves with

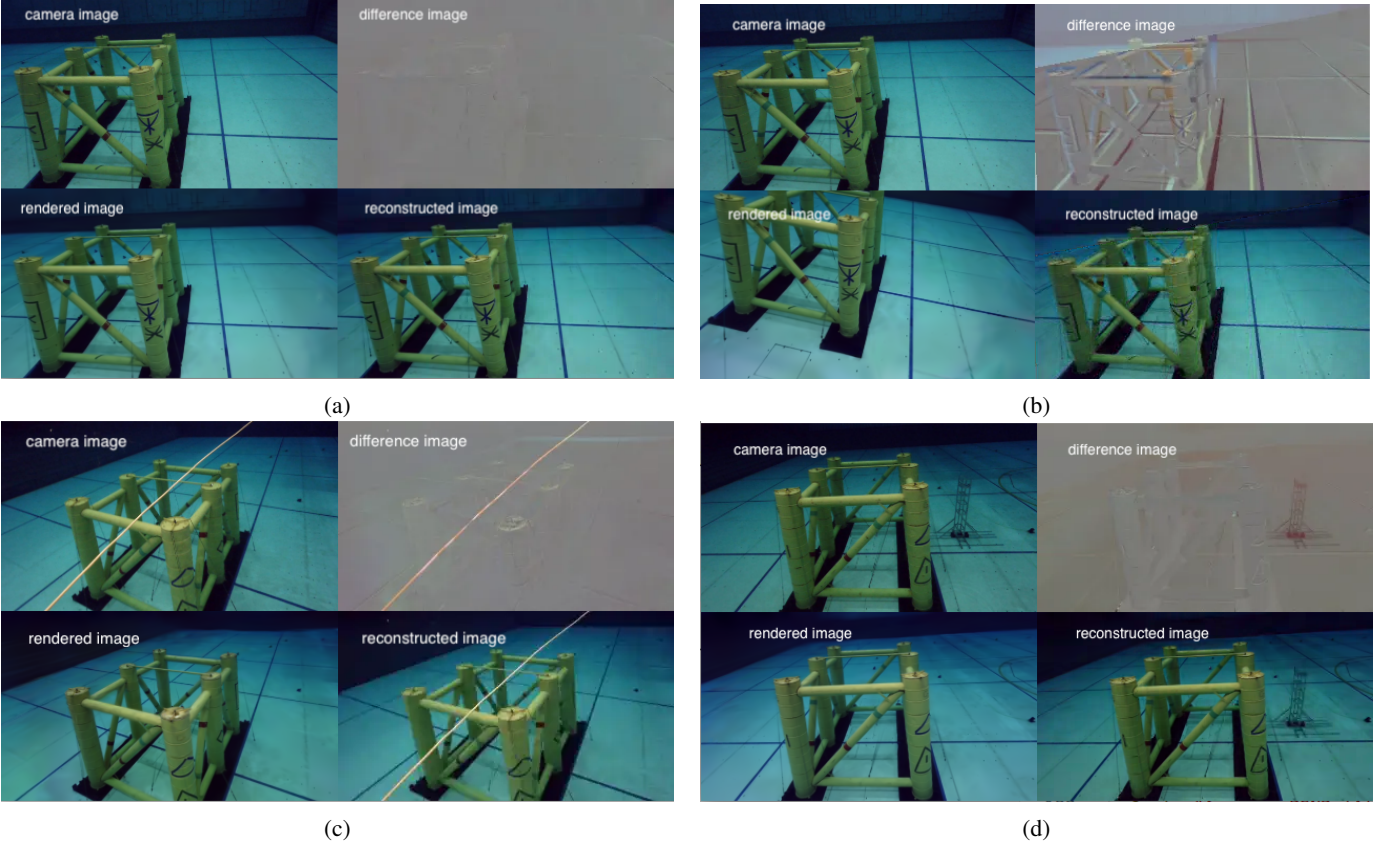


Fig. 9: Visualization of the results. Panel (a) shows the result of iNVS, panel (b) shows the result of Pose+3DGS+Compressor, panel (c) shows the result of the iNVS with the presence of a safety line and panel (d) shows the results of the iNVS with the presence of a new structure. We present the camera image, rendered image at the estimated latent representation, and the difference between the two images and the final reconstructed image.

the vehicle and appears on the camera, as shown in Fig. 9c. The second is a stationary metallic object with dimensions approximately $1.0 \text{ m} \times 0.25 \text{ m} \times 0.25 \text{ m}$, as shown in Fig. 4c. We find that iNVS handles both types of novel objects well. The average compressed data size with the presence of these objects is 1.65 kB, allowing us to transmit about 7 frames per second over a 100 kbps acoustic link. The results are summarized in Table I.

We find that even with the presence of novel objects in the scene, iNVS outperforms WebP and JPEG-XL both quantitatively and qualitatively. Specifically, iNVS using WebP as a subcomponent for compressing I_{diff} achieves a 2.39 times higher compression ratio than WebP and a 3.85 times higher compression ratio than JPEG-XL for T2. The PSNR of iNVS with JPEG-XL is 2.12 dB higher than WebP and 2.06 dB higher than JPEG-XL. From the visualization in Fig. 8b, the reconstructed images from iNVS are clearer and sharper than those obtained using classical compression methods.

Compared to the results in T1, the performance of iNVS degrades slightly in T2 due to two main reasons. First, the presence of a novel object in the scene increases the difficulty for the trained estimator to provide a good initialization. For the initial frames, we rely on the PoseLSTM estimator, as the rendered image from the previous frame is determined to be too different from the current frame, as shown by

its MSE which is greater than the threshold. As a result, the I_{diff} energies for the first few frames are larger due to less accurate pose initialization. Second, the presence of the novel object increases the entropy of I_{diff} , resulting in a larger compressed size. Nonetheless, the performance of iNVS remains significantly better than that of WebP and JPEG-XL, enabling near-real-time image transmission over limited-bandwidth acoustic links.

IV. CONCLUSION

In this paper, we propose a novel image compression approach based on iNVS for real-time image transmission over underwater acoustic links in inspection missions. Our technique is computationally efficient, and achieves higher compression ratios than classical lossy image compression techniques such as WebP. We evaluate the performance of different loss functions, optimization methods, and initialization methods for iNVS and demonstrate that MSE loss, BFGS based optimization, and the optimized pose of the previously acquired frame as the initialization are the most effective options. We evaluate the performance of our proposed technique in a confined underwater environment and demonstrate that it outperforms existing image compression techniques in terms of both compression ratio and image quality. We also examine the robustness of our method towards

novel objects in the scene and demonstrate that it can handle occlusion from both small and large structures. Overall, our iNVS technique outperforms WebP and JPEG-XL significantly and is a promising solution for real-time image transmission over limited-bandwidth acoustic links in inspection missions.

While iNVS is designed for underwater inspection missions, it can be applied to missions in other environments that require real-time image transmission over limited bandwidth, such as search and rescue missions in known environments with limited communication infrastructure. It can also be used for latent representation estimation in known environments, with high accuracy and robustness to small changes in the scene.

Future work will focus on improving the robustness of iNVS in handling dynamic changes in underwater scenes, such as varying lighting conditions and water turbidity, which are challenges commonly faced in at-sea environments. Additionally, we aim to extend iNVS for real-time video streaming, enabling efficient transmission of continuous visual data in underwater exploration. This extension will require further reducing the compressed data size while maintaining image quality and minimizing latency over acoustic communication links. Lastly, we will work towards a specialized image compressor for I_{diff} , as existing compressors are not necessarily optimal for this sparse, low-entropy data. A tailored solution could significantly reduce the size of the compressed I_{diff} and improve transmission efficiency.

ACKNOWLEDGMENT

This research project is supported by A*STAR under its RIE2020 Advanced Manufacturing and Engineering (AME) Industry Alignment Fund - Pre-Positioning (IAF-PP) Grant No. A20H8a0241.

REFERENCES

- [1] E. Vargas, R. Scona, J. S. Willners, T. Luczynski, Y. Cao, S. Wang, and Y. R. Petillot, "Robust underwater visual SLAM fusing acoustic sensing," in *2021 IEEE International Conference on Robotics and Automation (ICRA)*. IEEE, 2021, pp. 2140–2146. [Online]. Available: <https://ieeexplore.ieee.org/document/9561537/>
- [2] B. Bingham, B. Foley, H. Singh, R. Camilli, K. Delaporta, R. Eustice, A. Mallios, D. Mindell, C. Roman, and D. Sakellariou, "Robotic tools for deep water archaeology: Surveying an ancient shipwreck with an autonomous underwater vehicle," vol. 27, no. 6, pp. 702–717, 2010. [Online]. Available: <https://onlinelibrary.wiley.com/doi/10.1002/rob.20350>
- [3] M. Carreras, J. D. Hernandez, E. Vidal, N. Palomeras, and P. Ridao, "Online motion planning for underwater inspection," in *2016 IEEE/OES Autonomous Underwater Vehicles (AUV)*. IEEE, 2016, pp. 336–341. [Online]. Available: <http://ieeexplore.ieee.org/document/7778693/>
- [4] K. Shepherd, "Remotely operated vehicles (ROVs)*," in *Encyclopedia of Ocean Sciences (Second Edition)*, J. H. Steele, Ed. Academic Press, 2001, pp. 742–747. [Online]. Available: <https://www.sciencedirect.com/science/article/pii/B9780123744739003027>
- [5] A. D. Bowen, M. V. Jakuba, N. E. Farr, J. Ware, C. Taylor, D. Gomez-Ibanez, C. R. Machado, and C. Pontbriand, "An un-tethered roV for routine access and intervention in the deep sea," in *2013 OCEANS - San Diego*, 2013, pp. 1–7.
- [6] H.-P. Tan, R. Diamant, W. K. G. Seah, and M. Waldmeyer, "A survey of techniques and challenges in underwater localization," vol. 38, no. 14, pp. 1663–1676, 2011. [Online]. Available: <https://www.sciencedirect.com/science/article/pii/S0029801811001624>
- [7] M. Stojanovic and J. Preisig, "Underwater acoustic communication channels: Propagation models and statistical characterization," *IEEE Communications Magazine*, vol. 47, no. 1, pp. 84–89, 2009.
- [8] M. Chitre, S. Shahabudeen, L. Freitag, and M. Stojanovic, "Recent advances in underwater acoustic communications & networking," in *OCEANS 2008*, vol. 2008-Supplement, 2008, pp. 1–10.
- [9] N. Saeed, A. Celik, T. Y. Al-Naffouri, and M.-S. Alouini, "Underwater optical wireless communications, networking, and localization: A survey," *Ad Hoc Networks*, vol. 94, p. 101935, 2019. [Online]. Available: <https://www.sciencedirect.com/science/article/pii/S1570870518309776>
- [10] M. Y. I. Zia, J. Poncela, and P. Otero, "State-of-the-art underwater acoustic communication modems: Classifications, analyses and design challenges," vol. 116, no. 2, pp. 1325–1360, 2021. [Online]. Available: <https://doi.org/10.1007/s11277-020-07431-x>
- [11] T. Melodia, H. Kulhandjian, L.-C. Kuo, and E. Demirors, *Advances in Underwater Acoustic Networking*. John Wiley & Sons, Ltd, 2013, ch. 23, pp. 804–852. [Online]. Available: <https://onlinelibrary.wiley.com/doi/abs/10.1002/9781118511305.ch23>
- [12] G. Toderici, D. Vincent, N. Johnston, S. J. Hwang, D. Minnen, J. Shor, and M. Covell, "Full resolution image compression with recurrent neural networks," in *2017 IEEE Conference on Computer Vision and Pattern Recognition (CVPR)*. IEEE, 2017, pp. 5435–5443. [Online]. Available: <http://ieeexplore.ieee.org/document/8100060/>
- [13] J. Whang, A. Acharya, H. Kim, and A. G. Dimakis, "Neural distributed source coding," 2022, number: arXiv:2106.02797. [Online]. Available: <http://arxiv.org/abs/2106.02797>
- [14] A. Golinski, R. Pourreza, Y. Yang, G. Sautiere, and T. S. Cohen, "Feedback recurrent autoencoder for video compression," 2020. [Online]. Available: https://openaccess.thecvf.com/content/ACCV2020/html/Golinski_Feedback_Recurrent_Autoencoder_for_Video_Compression_ACCV_2020_paper.html
- [15] K. Gregor, F. Besse, D. J. Rezende, I. Danihelka, and D. Wierstra, "Towards conceptual compression," 2016. [Online]. Available: <http://arxiv.org/abs/1604.08772>
- [16] A. Sento, "Image compression with auto-encoder algorithm using deep neural network (DNN)," in *2016 Management and Innovation Technology International Conference (MITicon)*, 2016, pp. MIT-99–MIT-103.
- [17] L. Theis, W. Shi, A. Cunningham, and F. Huszár, "Lossy image compression with compressive autoencoders," 2017. [Online]. Available: <https://openreview.net/forum?id=rJiNwv9gg>
- [18] H. Liu, T. Chen, Q. Shen, T. Yue, and Z. Ma, "Deep image compression via end-to-end learning," in *CVPR Workshops*, 2018.
- [19] J. Ballé, D. Minnen, S. Singh, S. J. Hwang, and N. Johnston, "Variational image compression with a scale hyperprior," 2022. [Online]. Available: <https://openreview.net/forum?id=rkcQFMZRb>
- [20] S. Ma, X. Zhang, C. Jia, Z. Zhao, S. Wang, and S. Wang, "Image and video compression with neural networks: A review," vol. 30, no. 6, pp. 1683–1698, 2020, conference Name: IEEE Transactions on Circuits and Systems for Video Technology.
- [21] B. Mildenhall, P. P. Srinivasan, M. Tancik, J. T. Barron, R. Ramamoorthi, and R. Ng, "NeRF: Representing scenes as neural radiance fields for view synthesis," 2020. [Online]. Available: <http://arxiv.org/abs/2003.08934>
- [22] B. Kerbl, G. Kopanas, T. Leimkuehler, and G. Drettakis, "3d gaussian splatting for real-time radiance field rendering," vol. 42, no. 4, pp. 1–14, 2023. [Online]. Available: <https://dl.acm.org/doi/10.1145/3592433>
- [23] R. Mishra, M. Chitre, B. Kalyan, Y. M. Too, H. Vishnu, and L. Peng, "An architecture for virtual tethering of rovs," in *OCEANS 2024 - Singapore*, 2024, pp. 1–6.
- [24] L. Peng, H. Vishnu, M. Chitre, Y. M. Too, B. Kalyan, R. Mishra, and S. P. Tan, "Pose estimation from camera images for underwater inspection," 2024. [Online]. Available: <http://arxiv.org/abs/2407.16961>
- [25] L. Peng and M. Chitre, "Regressing poses from monocular images in an underwater environment," in *OCEANS 2022 - Chennai*, 2022, pp. 1–4. [Online]. Available: <https://ieeexplore.ieee.org/abstract/document/9775281>
- [26] L. Peng, H. Vishnu, M. Chitre, Y. M. Too, B. Kalyan, and R. Mishra, "Improved image-based pose regressor models for underwater environments," 2024. [Online]. Available: <http://arxiv.org/abs/2403.08360>
- [27] L. Yen-Chen, P. Florence, J. T. Barron, A. Rodriguez, P. Isola, and T.-Y. Lin, "iNeRF: Inverting neural radiance fields for pose estimation," in *2021 IEEE/RSJ International Conference on Intelligent Robots and Systems (IROS)*, 2021, pp. 1323–1330, ISSN: 2153-0866.
- [28] Y. Sun, X. Wang, Y. Zhang, J. Zhang, C. Jiang, Y. Guo, and F. Wang, "iComMa: Inverting 3d gaussian splatting for camera pose estimation via comparing and matching," 2024, version: 2. [Online]. Available: <http://arxiv.org/abs/2312.09031>
- [29] D. P. Kingma and J. Ba, "Adam: A method for stochastic optimization," 2017. [Online]. Available: <https://arxiv.org/abs/1412.6980>

- [30] C. G. Broyden, "The Convergence of a Class of Double-rank Minimization Algorithms 1. General Considerations," *IMA Journal of Applied Mathematics*, vol. 6, no. 1, pp. 76–90, 03 1970. [Online]. Available: <https://doi.org/10.1093/imamat/6.1.76>
- [31] R. Fletcher, "A new approach to variable metric algorithms," *The Computer Journal*, vol. 13, no. 3, pp. 317–322, 01 1970. [Online]. Available: <https://doi.org/10.1093/comjnl/13.3.317>
- [32] D. Goldfarb, "A family of variable-metric methods derived by variational means," *Mathematics of Computation*, vol. 24, no. 109, pp. 23–26, 1970. [Online]. Available: <http://www.jstor.org/stable/2004873>
- [33] D. F. Shanno, "Conditioning of quasi-newton methods for function minimization," *Mathematics of Computation*, vol. 24, no. 111, pp. 647–656, 1970. [Online]. Available: <http://www.jstor.org/stable/2004840>
- [34] V. Ye and A. Kanazawa, "Mathematical supplement for the `gsplat` library," 2023.
- [35] M. Tancik, E. Weber, E. Ng, R. Li, B. Yi, J. Kerr, T. Wang, A. Kristoffersen, J. Austin, K. Salahi, A. Ahuja, D. McAllister, and A. Kanazawa, "Nerfstudio: A modular framework for neural radiance field development," in *ACM SIGGRAPH 2023 Conference Proceedings*, ser. SIGGRAPH '23, 2023.
- [36] J. L. Schönberger, E. Zheng, J.-M. Frahm, and M. Pollefeys, "Pixelwise view selection for unstructured multi-view stereo," in *Computer Vision – ECCV 2016*, B. Leibe, J. Matas, N. Sebe, and M. Welling, Eds. Springer International Publishing, 2016, pp. 501–518.
- [37] R. Feinman, "Pytorch-minimize: a library for numerical optimization with autograd," 2021. [Online]. Available: <https://github.com/rfeinman/pytorch-minimize>
- [38] J. Sun, Z. Shen, Y. Wang, H. Bao, and X. Zhou, "LoFTR: Detector-free local feature matching with transformers," 2021. [Online]. Available: <http://arxiv.org/abs/2104.00680>
- [39] TCOMS, "RESEARCH & DEVELOPMENT ON OCEAN SYSTEMS AND SOLUTIONS." [Online]. Available: <https://www.tcoms.sg/research-development/>